Journal of
Sedimentary
Research

Journal of Sedimentary Research, 2020, v. 90, 1–13
Research Article
DOI: http://dx.doi.org/10.2110/jsr.2020.37

LINKING MARINE CORE LITHOFACIES AND MINERAL AND GRAIN-SIZE COMPOSITIONS ON THE BAFFIN ISLAND MARGIN: CHANGES IN PROVENANCE AND TRANSPORT

JOHN T. ANDREWS,[1] KIMBERLEY JENNER,[2] AND CALVIN CAMPBELL[2]
[1]*INSTAAR and Department of Geological Sciences, 4001 Discovery Drive, University of Colorado, Boulder, Colorado 80303, U.S.A.*
[2]*Geological Survey of Canada–Atlantic, 1 Challenger Drive, Dartmouth, Nova Scotia B2Y 4A2, Canada*
e-mail: andrewsj@colorado.edu

ABSTRACT: **We evaluate the linkages between lithofacies and mineral composition of late Quaternary sediments along the Baffin Slope for cores 2013029 64, 74, and 77. Four major lithofacies were identified: diamicton (L1), laminated red-brown mud (L2), tan carbonate mud (L3), and brown bioturbated mud (L4). In addition, gold-brown mud (L2a) beds were identified within red-brown mud throughout the Baffin margin and a thin, locally distributed light gray mud (L2b), also identified within red-brown mud, was localized to the Home Bay region. A classification decision tree (CDT) correctly predicted ∼ 87% of the lithofacies based on five binary choices based on the estimated weight %s of (in order): quartz, kaolinite, plagioclase, iron oxides, and smectites. The detrital tan carbonate (DC) minerals, calcite and dolomite, did not appear in the chosen CDT solution although this lithofacies is easily recognized in cores because of its tan color and the facies is well predicted in the CDT. The addition of grain size did not substantially improve the prediction of the lithofacies although it did change the % importance of the minerals in the CDT.**

INTRODUCTION

In two recent papers, Andrews et al. (2014, 2018) documented Baffin Bay sediment mineralogy of seafloor and core samples and the variation in core lithofacies along the Baffin Island margin was described and interpreted (Jenner et al. 2018). In this short paper we seek to determine if there is a predictable association between the lithofacies and their mineralogy based on the mineralogical results from quantitative X-ray-diffraction (qXRD) analyses. Our investigation is based on three cores from the Baffin slope (Fig. 1A, B) collected during cruise HU2013029, namely cores 64, 74, and 77 (Jenner et al. 2018). The available radiocarbon dates from the three cores (Jenner et al. 2018) indicate that they record along-slope deposition from roughly the present day (core top dates not available because of carbonate dissolution; Azetsu-Scott et al. 2010; Andrews and Eberl 2011) to a time before the opening of the Canadian Arctic channels.

Variations in the mineral composition of lithofacies can be driven by two, possibly linked, processes: 1) changes in sediment provenance, and/or 2) changes in grain size. Changes in the provenance of glacial marine sediments in western Baffin Bay were driven by the dynamics and variable dominance and extent of the numerous ice streams and ice sheets that fronted the Baffin Island margin (Dyke et al. 2002; Margold et al. 2014, 2015a). Sediment grain-size variability was associated with changes in the factors controlling the transport and deposition of sediment, especially in areas influenced by iceberg rafting, suspended-sediment delivery, and bottom currents (Aksu and Piper 1987; Prins et al. 2002; Rebesco et al. 2014; Hesse 2016; McCave et al. 2017; Jenner et al. 2018; McCave and Andrews 2019a, 2019b).

METHODS

We describe our methodology for characterizing the lithofacies, obtaining weight percentage (wt%) estimates for the < 2 mm sediment mineral composition, and determining grain size.

Lithofacies

Four of the six lithofacies, diamicton (L1), laminated red-brown mud (L2), tan carbonate gravelly, sandy mud (L3), and bioturbated brown mud (L4), included in the classification decision tree are adapted from Jenner et al. (2018). The additional two lithofacies, gold-brown mud (L2a) and light gray mud (L2b) were presented in Jenner et al. (2018) but were not developed separately. The stratigraphic succession of all lithofacies is presented in Figure 2. Dark gray-brown matrix-supported L1, interpreted as glacigenic debris-flow deposits (GDFD), is found at the base of cores 64 and 74 and consists of poorly sorted gravelly, sandy mud. L1 is overlain by laminated L2, deposited from a combination of meltwater-plumes and turbidity currents. L2 occurs stratigraphically above L1 in cores 64 and 74 and at the base of core 77. L2 contains beds (< 10 cm thick) and laminae of L2a, throughout Baffin margin HU2013029 cores, and intervals (< 30 cm) of L2b in the Home Bay region. L2a–b are illustrated in this research because of their unique color, which perhaps represents a specific sediment source. L2a was identified within L2 only in cores 64 and 77. The similarly laminated nature of L2a and L2 is suggestive of both meltwater-plume and turbidity-current deposition. L2b was identified in core 74, between L1 and L3, and in core 77 beneath L3. The mottled appearance of some beds in L2b in addition to the potential for influence by the Baffin Island Current, which extends down to 1200 m, suggests that L2b may have been influenced by bottom currents. Poorly sorted L3, interpreted as ice-rafted-

Published Online: Month 2020
Copyright © 2020, SEPM (Society for Sedimentary Geology) 1527-1404/20/090-000

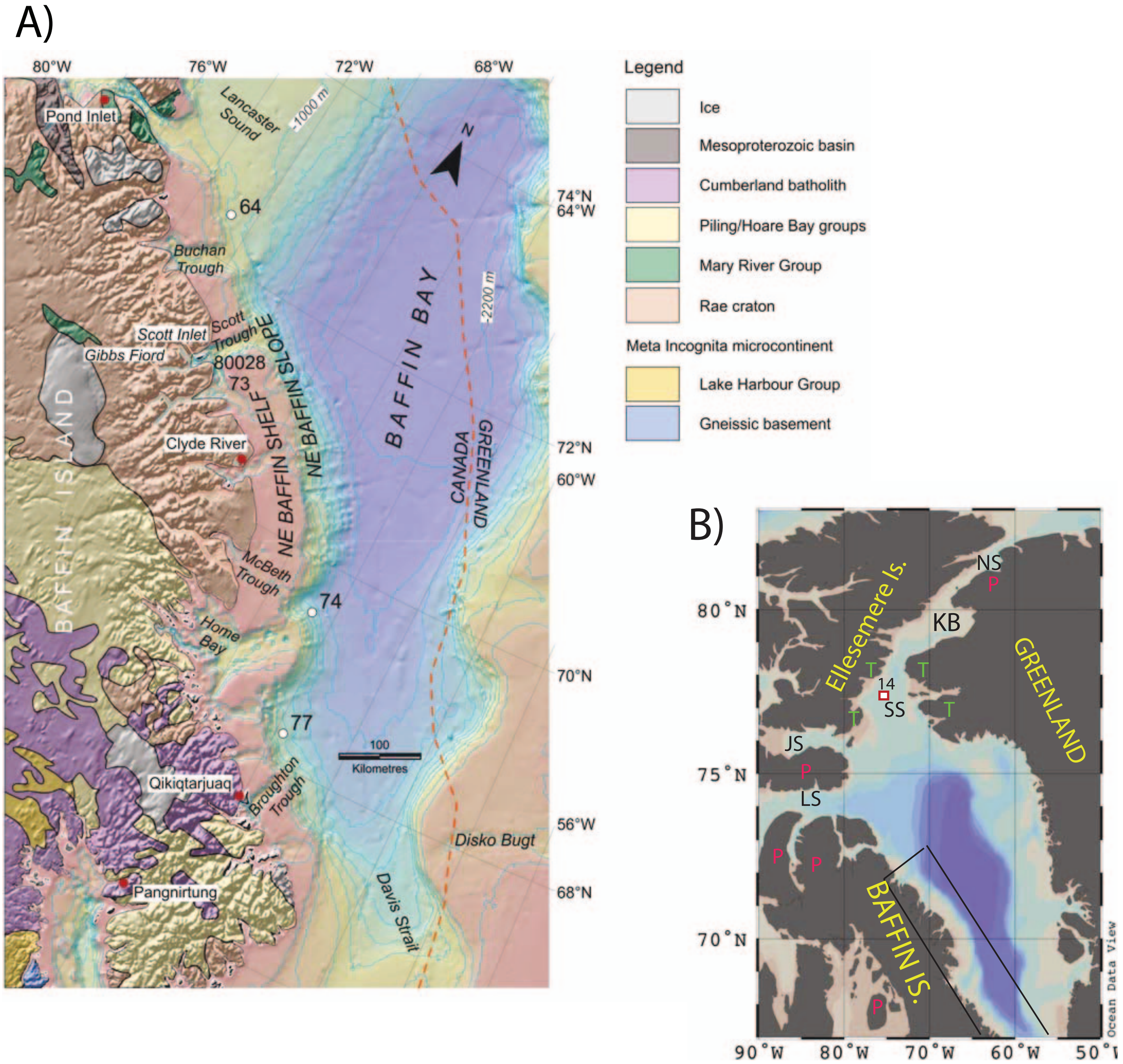

FIG. 1.—**A)** Cruise 2013029 core locations and bedrock geology of Baffin Island adapted from St-Onge et al. (2009). **B)** Location of the core sites (black rectangle) in the context of Baffin Bay, W–NW Greenland, and the Canadian Arctic islands and channels. LS, Lancaster Sound; JS, Jones Sound; SS, Smith Sound; KB, Kane Basin; NS, Nares Strait; P (red), carbonate outcrops; T (green), Thule Supergroup.

deposition, is younger than L2 and occurs as a couplet in all three cores, thinning from north (64) to south (77). L3 is equivalent to the detrital-carbonate events of Aksu (1981), Andrews et al. (1998), and Jennings et al. (2018). Bioturbated Holocene mud (L4), interpreted as hemipelagic sedimentation, is found at the tops of all cores.

Quantitative X-Ray Diffraction (qXRD)

A total of 202 samples from trigger weight (TWC) and piston cores (PC) were prepared using the method outlined by Eberl (2003), in which 10% by weight of zincite is added to 1 g of sediment < 2000 μm. Samples are ground, dried, and processed on a Siemens D5000 X-ray diffractometer with a 2 sec scan every 0.02° 2-θ for the interval between 5° and 65° 2-θ, generating 3000 intensity records. The weight % of minerals in the sample is estimated by means of the Excel macro program Rockjock v6 (Eberl 2003). Issues involving estimates of errors using this method have been discussed in several papers (Andrews et al. 2015, 2018; Raven and Self 2017).

Although we routinely derive wt% estimates for some 34 minerals (including nine feldspars) out of a total of 124 standards included in Rockjock v6 (Table 1), we reduce the number of minerals by amalgamating the minerals into 13 groups (Table 1), for example, grouping minerals

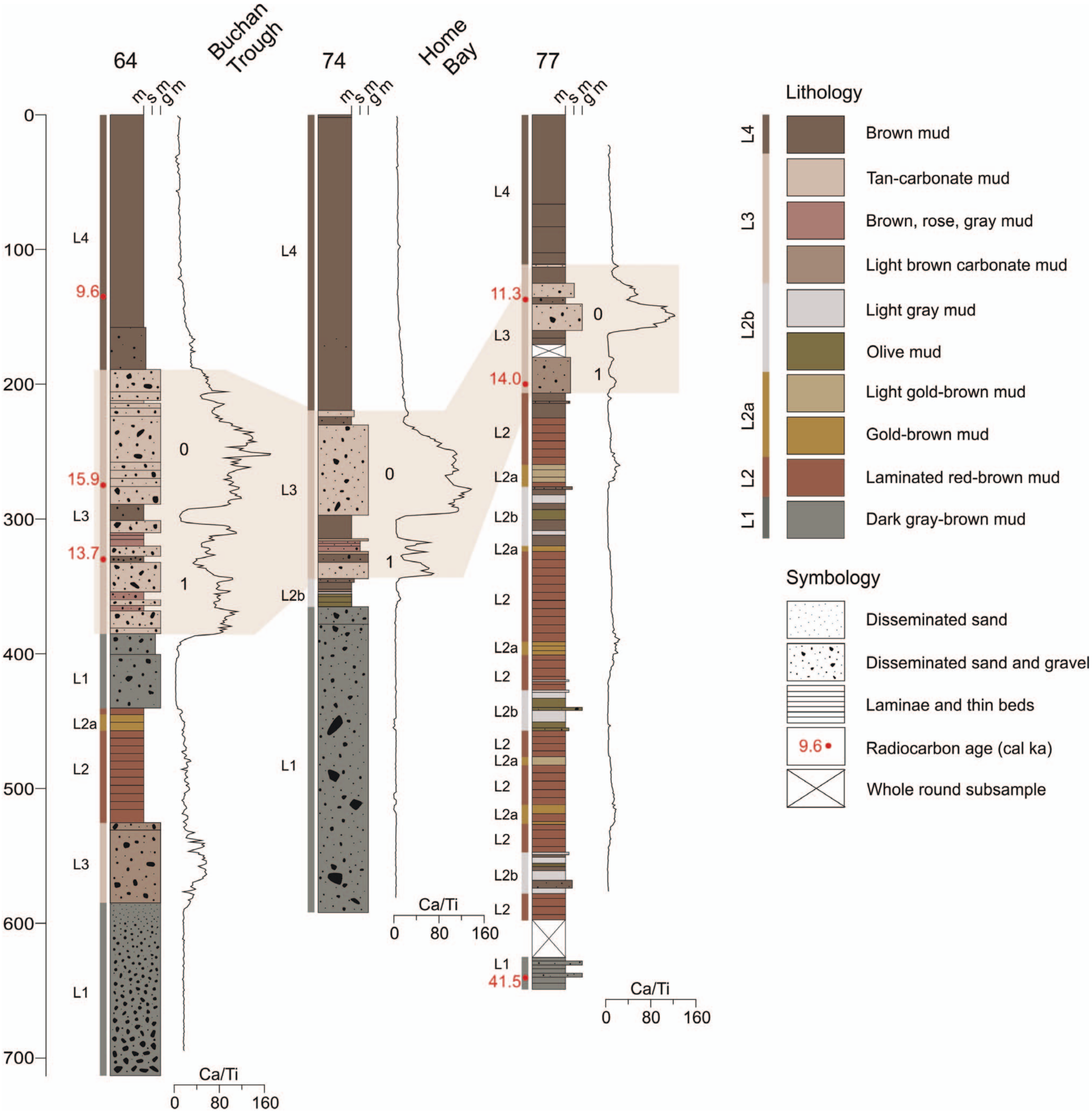

FIG. 2.—Lithofacies succession and Ca/Ti portable X-ray fluorescence profiles for cores HU2013029 64, 74, and 77 (after Jenner et al. 2018; see Fig. 1 for core locations). Detrital tan carbonate mud events of Andrews et al. (1998) are highlighted.

albite to anorthite into plagioclase. We group dolomite and ferroan dolomite into a single category, but it is worth noting that the downcore changes in these two variants may contain clues about regional provenance, although detailed bedrock mapping would be required to decode the signal.

Grain-Size Analysis

Detailed laser grain-size analyses of reserve samples from qXRD (see above) were obtained for cores 64 and 77 using a Malvern 3000 instrument, which obtains volume wt% estimates between 2000 and 0.4 µm (McCave and Andrews 2018, 2019). Samples were sieved through a 2 mm mesh and the wt% of sediment > 2 mm was recorded. One gram of sediment < 2 mm was then prepared for detailed grain-size analysis. The 74 grain-size bins were entered into the Excel macro program Gradistat (Blott and Pye 2001) to obtain estimates on grain-size characteristics, such as median grain size, % sand, or % very coarse silt (Table 1). We are aware that sampling of sediment tends to under report the presence of gravel-size clasts, and have conducted experiments to evaluate the extent of the problem (Andrews and Roth, in prep).

Thus, both the qXRD and grain-size data are based on the bulk sediment < 2000 µm and the gravel fractions are not included in any analysis, although they are considered as part of the lithofacies.

TABLE 1.—List of minerals initially listed in Rockjock v6 and the reduced list used in this paper, and list of the grain size classification and their limits (µm).

	Initial search	#identification	Reduced list	Grain-size parameters	µm range
Sample name:					
Full pattern degree of fit:					
Mineral					size µm
NON-CLAYS					
Quartz	1	1	Quartz	% v fine gravel	> 2000
Ordered microcline feldspar	2	2 to 5	alkfel	% v coarse sand	1000
Intermediate microcline feldspar	3	6 to 10	plag	% coarse sand	500
Orthoclase feldspar	4	18 to 21	FeO	% medium sand:	250
Anorthoclase feldspar	5	23 and 24	SiO	% fine sand	125
Albite feldspar (Cleavelandite)	6	11	Calcite	% v fine sand	63
Oligoclase feldspar (Norway)	7	12 and 13	dolomite	% v coarse silt	31
Labradorite feldspar	8	16	Amphibole	% coarse silt	16
Bytownite feldspar	9	17	Pyroxene	% medium silt	8
Anorthite feldspar	10	25	Kaolinite	% fine silt	4
Calcite	11	26 to 28	smectites	% v fine silt	2
Dolomite	12	29,30,33,34	illites	% clay	< 2
Fe-Dolomite	13	31 and 32	biochlor		
Siderite	14				
Halite	15				
Amphibole (ferrotschermakite)	16				
Pyroxene (diopside)	17				
Pyrite	18				
Magnetite	19				
Hematite	20				
Maghemite	21				
Diatoms	22				
Chert (8.4 nm)	23				
Total non-clays					
CLAYS					
Kaolinite (Dry Branch)	25				
Saponite	26				
Ferruginous smectite	27				
1Md illite (+ dioct mica and smectite)	28				
1M Illite (R > 2; 88%I)	29				
1M illite (R > 1, 70–80%I)	30				
Biotite (2M1)	31				
Fe-chlorite (Tusc)	32				
Muscovite (2M1)	33				
Illite (1M, PD3B)	34				
Total clays					
TOTAL					

BACKGROUND, AND BEDROCK AND SEDIMENT-TRANSPORT CONTROLS

During the last glacial maximum (LGM) the Laurentide, Greenland, and Innuitian ice sheets extended to the shelf breaks (Dyke et al. 2002; Li et al. 2011; Jennings et al. 2017a; Brouard and Lajeunesse 2017) and ice streams flowed into northern Baffin Bay from the Canadian Arctic channels (Marshall and Clarke 1996; MacLean et al. 2010; Margold et al. 2015a, 2015b). Glacial mass-flow deposits, meltwater sediment plumes, and iceberg rafting of sediments were the principal sediment transport mechanisms (Aksu and Piper 1987; Aksu and Hiscott 1989; Jenner et al. 2018) and sediment mineral compositions were governed by glacial erosion of the widespread Precambrian Shield bedrock dominated by quartz and feldspars (Fig. 1A). However, given the location of the LGM terminus (Li et al. 2011), deglacial events were initially recorded as distinct detrital carbonate facies (Aksu 1985; Andrews et al. 1998; Piper 1973) reflecting retreat of the ice streams into the Canadian Arctic islands and channels composed of Paleozoic carbonates, principally dolomites (Parnell et al. 2007) (Fig. 1B). Further retreat, especially northward to Smith Sound and Nares Strait, would initially expose sediments, especially red beds, of the Thule Supergroup (Dawes 1997) as well as Cambrian and Devonian carbonates (Fig. 1B). Minerals indicative of subaerial weathering, such as kaolinite and smectite, are sourced in relatively limited Cretaceous and Tertiary outcrops on land and in marine basins (MacLean et al. 2011, 2014; Bennett et al. 2014). Deglacial sediment transport to our now distal (to ice margins) core sites (Fig. 1A, B) require long-distance transport by icebergs and water or reworking by mass wasting (glacial debris-flow deposits), bottom currents, and iceberg scouring.

COMPARISON OF LITHOFACIES MINERAL COMPOSITION AND GRAIN SIZE

The question we address is: Are the various lithofacies that characterize sediments along the Baffin slope (Fig. 2) associated with specific minerals and/or grain-size attributes? We use "machine learning" approaches (Gorunescu 2011; Zumel and Mount 2014; Kabacoff 2015) to investigate to what extent each lithofacies can be explained or predicted by mineral and/or grain-size compositions. To a degree, both of these components enter into the lithofacies determinations (Jenner et al. 2018) but it is unclear whether significant changes in sediment composition occur during transport along the slope or from the discrete contributions of numerous intervening fiord ice streams (Fig. 1). We use the classification decision tree (CDT) approach (Vermeesch 2006; Gorunescu 2011; Koseoglu et al. 2018a, 2018b; Andrews 2019) to evaluate if there is a predictable relationship between mineral composition and/or grain size. The analyses are carried out in R (https://www.r-project.org) using R packages: rpart, rpart.plot, and randomForest.

Lithofacies and Mineral Composition (Cores 64, 74, 77)

We used 203 samples from cores 64PC, 74PC, and 77TWC, and PC, representing six lithofacies: Holocene mud (L4), tan carbonate mud (L3), red-brown mud (L2), gold- brown mud (L2a), light gray mud (L2b), and basal diamicton (L1) (adapted from Jenner et al. 2018). The appropriate number of binary decisions in a CDT, in our case the lithofacies classification, is judged by a plot of the complexity parameter (cp) versus the relative error; essentially a cost–benefit analysis (Fig. 3A). This determines the number of branches (i.e., decisions) on the CDT and balances the conflict between obtaining the best prediction versus minimizing the binary choices. In our study the crossing point has a cp $= 0.024$, resulting in six binary choices. The first choice is whether the wt% of quartz is $< 19\%$. If the answer is "no," then the link to the right identifies the outcome as basal diamicton (L1, see also Fig. 4). The remaining five lithofacies are linked to a "yes" decision (to the left on the CDT). L3, although normally considered a "detrital carbonate" facies (Andrews et al. 1998; Jenner et al. 2018), in the CDT approach is distinguished from the other facies by having low wt% of kaolinite (Fig. 4). L4, L2, and L2b are delimited by binary choices based on the wt % of plagioclase, iron oxides, and smectites (Figs. 3, 4). L2a is thin and intermittent and was not considered in the CDT. The meaning of the percentages in and outside the nodes is shown in the example in Figure 3A (thus 43 out of 47 diamictons are defined by > 19 wt% quartz, of which 38 were originally designated as L1, but the > 19 wt% quartz also includes 1, 2, and 2 samples, respectively, from L3, L2b, and L2). Figure 4 shows a boxplot of the key minerals for each of the six lithofacies. We have also included the carbonate weight % (calcite + dolomite); this figure indicates that all facies have some carbonate but the median wt% for all but the tan carbonate facies are close to 0%. Given the limited number of samples, it is difficult to define a specific mineral composition for L2a (gold-brown mud). However, the boxplots (Fig. 4) indicate those samples have the highest iron-bearing mineral median % and second-highest smectite median wt%.

A result of the CDT approach is an analysis of the agreement between the original and predicted lithofacies. A contingency table (Fig. 3B, Table 2A) shows that 82% of the lithofacies were correctly classified, and the contingency coefficient (C) (Siegel 1956) of $C = 0.86$ indicates that the null hypothesis of no association between observed and predicted lithofacies can be rejected at $p < 0.0001$. The importance of individual minerals in the various CDTs is illustrated in Figure 5. There is a slight change in the percentages when core 74 is excluded, but the most important minerals ($> 10\%$) for all three cores are quartz, plagioclase, kaolinite, and amorphous and fine grained silica (Fig. 5A).

CDTs can be affected by outliers, and to check the robustness of these results, and to gain additional information, we employed an ensemble approach using the R package "randomforest." In this ensemble approach 500 random selections were made of the 203qXRD samples and a "confusion table" (that is a contingency table) shows the degree of agreement between the original lithofacies counts and those predicted by the ensemble approach (Table 2B). Holocene muds (L4) are extremely well predicted as are the basal diamictons (L1), whereas the poorest prediction is for gold-brown mud (L2a) (Table 2B, class error). The importance of the minerals in terms of the predicted lithofacies is measured by two methods (Fig. 5D), both indicate the importance of quartz, followed by kaolinite, plagioclase, iron oxides, and smectites.

Relative Importance of Grain Size and Mineralogy in Lithofacies (Cores 64, 77)

We have shown that mineral compositions explain a large fraction of the sampled lithofacies; however, the recognition of lithofacies also includes a consideration of grain size. We will next evaluate the importance of this versus mineral composition for the NE Baffin Slope lithofacies (Jenner et al. 2018). Grain-size data are not available for core 074, but we have 101 samples from cores 64 and 77 (Fig. 1) with estimates of the percentages of sediment in the range from very fine gravel (< 2 mm) to clay (< 0.45 μm) (Table 1); the absence of estimates of a size > 2 mm should be noted and might explain some of the weakness in the predictions. The CDT for the association between grain size and lithofacies (Fig. 6A) is much weaker than the lithofacies and mineral linkage (Table 2C, $C = 0.65$), and L2a and L2b were not identified as having any distinctive grain-size attributes. The contingency-table results (Table 2C) indicate a non-random association, but correctly classified only 61 out of 101 lithofacies, indicating that 40% of them were misclassified. The first binary choice (% fine sand (FSN) $<$ 4.8%) separates L3 and L1 (= no) from L2a and L2b (= yes). The other major grain-size descriptors are coarse silt (%CSI), very fine silt (%VFSI), and very coarse silt (%VCSI) (Fig. 6A).

Next, we evaluate the importance of minerals and grain size on cores 64 and 77. By excluding 074 we noted some modest, but not radical, changes in the importance of the minerals as compared to the results from all three cores (Figs. 4, 5C, 6B). Thus, although we lack grain size data from core 74, we suggest that that will not affect the overall conclusions that can be drawn from cores 64 and 77. The complexity parameter suggests that a CDT of size 4 ($cp = 0.12$) has the best cost–benefit. What is striking (Fig. 6B) is that although no grain-size parameter is included in this CDT, the ranking of the mineral importance is quite different from when only the mineral data is considered (Fig. 5B), with dolomite, calcite, pyroxene, and quartz contributing the most to the CDT, and the importance of kaolinite is reduced. The inclusion of mineralogy resulted in only 16 samples being misclassified (Table 2D), thus indicating a significant improvement, with a value of $C = 0.85$, over the use of grain-size data alone (Table 2C) versus 0.65 with grain size alone. In addition, the joint qXRD and grain-size predictions now include lithofacies L2, which was not recognized in the grain-size analysis (Table 2C).

DISCUSSION

The association between sediment mineral compositions and lithofacies (Table 2A, Fig. 5) indicates that the lithofacies succession may be associated with changes in sediment sources and depositional processes (Andrews et al. 2018; Jenner et al. 2018). The CDT based on wt% is biased toward those minerals with the largest contributions (Fig. 5). This may hide important changes in those minerals with smaller contributions. To test this we scaled the data (0 to 1) (Miesch 1976) so that each mineral has an equal weight. The result (not shown) revealed very little difference in either the importance of a mineral or in the CDT. This indicates that the original CDT contains most of the important information in terms of the association between lithofacies and mineral composition. The plot of the important mineral wt% and lithofacies indicate the following connections (see also Fig. 4).

L4: low in quartz and calcite, high in smectite
L3: high in dolomite and calcite, low in biotite and chlorite
L2b: high in plagioclase and smectites, low in dolomite
L2: high in kaolinite
L2a: not entered
L1: high in quartz

The significance of differences in mineral wt% between the lithofacies was evaluated by the *post hoc* Scheffe test (Table 3). A simple metric of the

A)

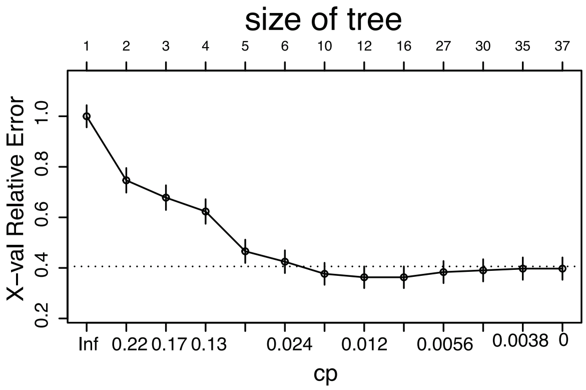

B)

Two-Way Contingency Table

Lithofacies	L4	L3	L2b	L2	L2a	L1
Predict facies						
L4	53	0	0	0	0	1
L3	4	30	1	0	1	0
L2b	0	3	22	0	0	4
L2	0	6	1	20	10	1
L2a						
L1	0	1	2	2	0	40

df = 20 Calc. Chi-sq = 552.47 p= < 0.0001

Chi-sq 0.01 = 37.56

C) Lithofacies. n = 203

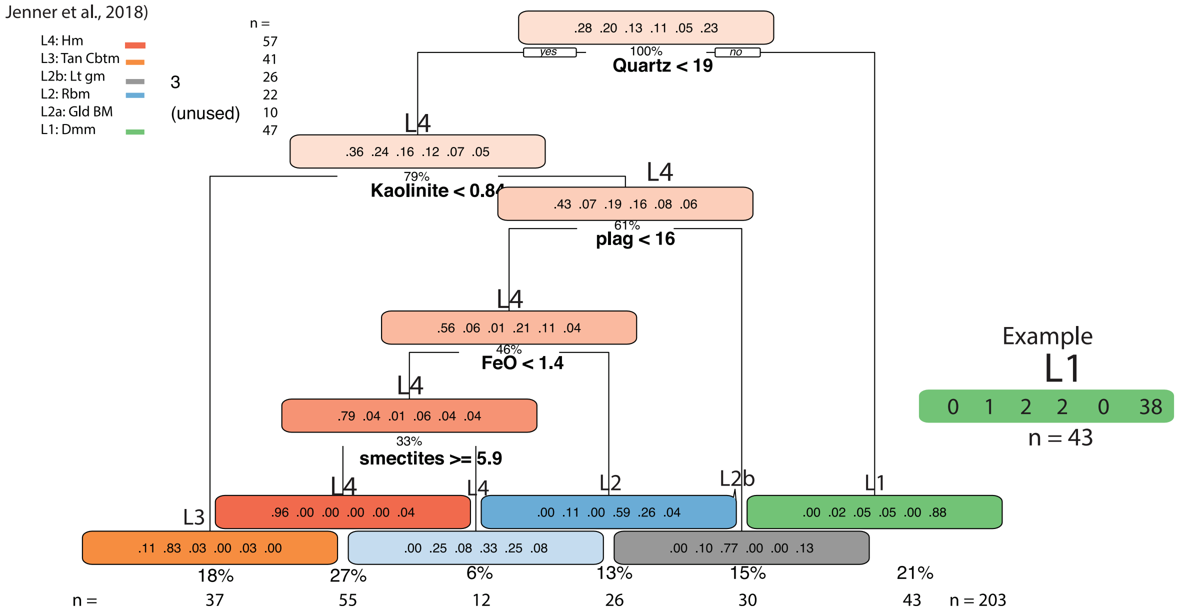

FIG. 3.—Classification decision tree analysis of the association between the lithofacies (Fig. 2) and mineral content (Table 1). **A)** cost-benefit analysis on the size of the tree—choice = 0.02. **B)** Contingency Table of the degree of similarity between the defined versus predicted lithofacies. Figures in red are the counts of a correct outcome. **C)** Classification decision tree for the lithofacies and mineral association. Note that L2a (gold-brown mud) had too small a representation to be considered.

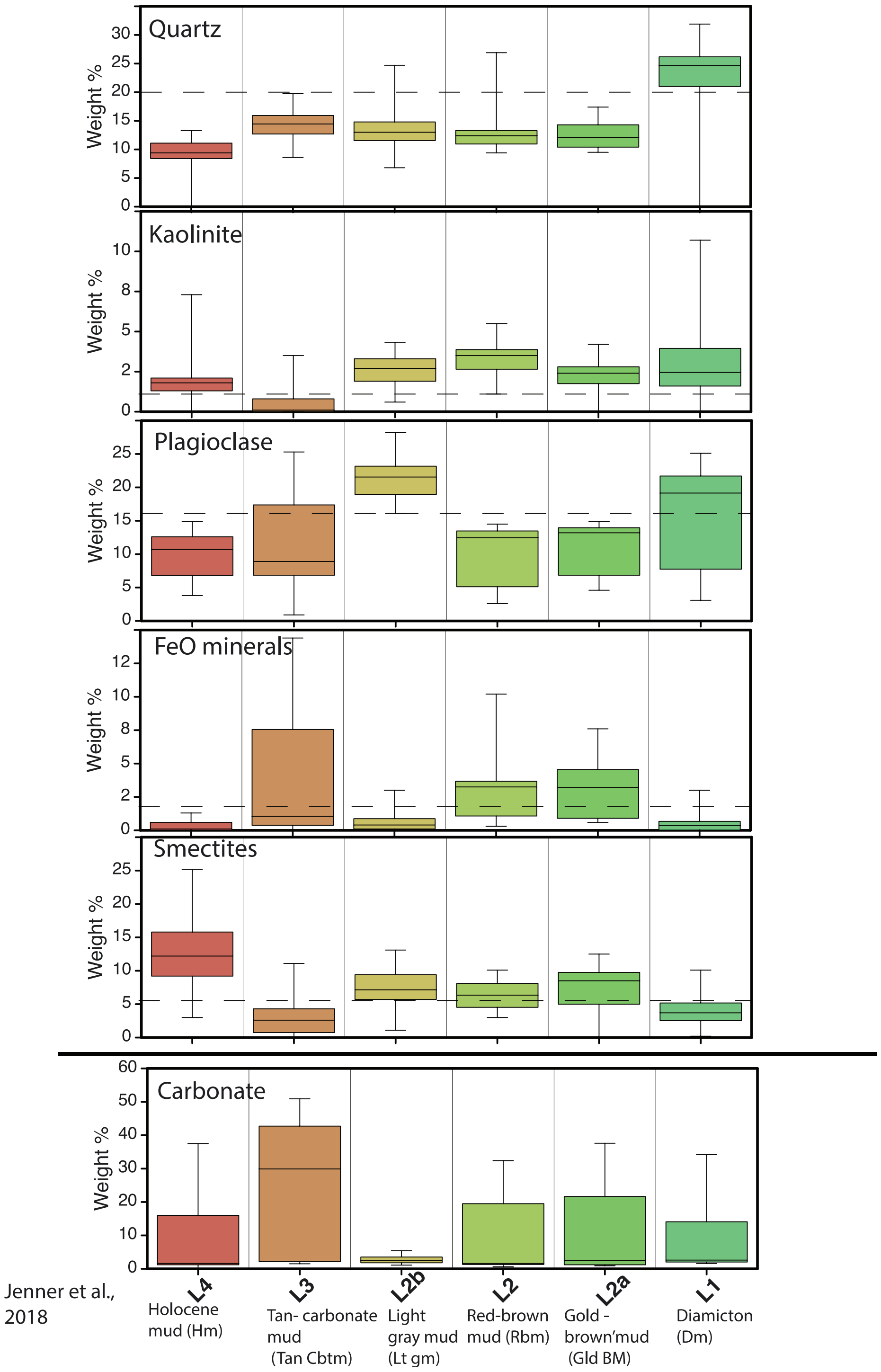

FIG. 4.—Boxplot of the weight% data for those minerals contributing to the classification decision tree (Fig. 3C), plus carbonate wt%. The solid line in each box is the median weight%, and the box includes the range of 50% of the distribution. The dashed line for each mineral represents the critical binary choice noted in Figure 3C. Lithofacies designations are adapted from Jenner et al. (2018).

degree of significant differences between lithofacies mineralogy is the number of significant differences between them (Table 3) and the five most important minerals in the CDT (Fig. 3C). There are five comparisons per lithofacies, hence a total of 25 comparisons per comparison. Table 3 indicates that the Holocene mud (L4) and the grey diamicton (L1) are the most different from the other lithofacies. The tan carbonate mud, L3, (i.e., the detrital-carbonate events of earlier studies (Aksu 1981; Aksu and Mudie 1984; Andrews et al. 1998; Simon et al. 2014)) is the third-most distinctive; the lithofacies that is least distinctive is gold-brown mud (L2a), possibly because of the limited number of samples (n = 10).

We argue that the lithofacies sequence (Figs. 2, 7) is recording the phasing of events associated with the late Quaternary deglaciation of northern Baffin Bay, and then the opening of the Canadian Arctic channels (CAC), especially Smith Sound and Nares Strait (Jennings et al. 2011, 2018; Li et al. 2011; Furze et al. 2018; Georgiadis et al. 2018). With the margin of the Foxe Dome of the Laurentide Ice Sheet at or close to the shelf break during the Last Glacial Maximum (LGM) (Brouardand

TABLE 2.—Contingency table of the agreement between the lithofacies and the predicted lithofacies derived from the A) 203 mineral matrix, B) the randomForest output, and C) Contingency Table for the lithofacies association with grain size in cores 64 and 77.

A)

Lithofacies Predict qXRD 064, 074, 077	L4	L3	L2a	L2	L2b	L1
L4	**53**	0	0	0	0	1
L3	4	**30**	1	0	1	0
L2a	0	3	**23**	0	0	4
L2	0	6	1	**20**	10	1
L2b						
L1	0	1	2	2	0	**40**
df = 30	Chi-sq = 627.02		p = < 0.0001			
	Chi-sq p 0.01; = 50.89			C = 0.86		

B)

Confusion Table: randomForest

Predict qXRD 064, 074, 077	L4	L3	L2a	L2	L2b	L1	class.error
L4	**53**	4	0	0	0	0	0.07
L3	0	**33**	3	2	2	0	0.175
L2a	1	1	**20**	0	1	4	0.259
L2	0	1	0	**19**	1	1	0.136
L2b	1	2	0	4	**3**	1	0.727
L1	0	2	4	0	1	**38**	0.156
Original	55	43	27	25	8	44	202
Matched%	**96.4**	**76.7**	**74.1**	**76**	**37.5**	**86.4**	**82.2**

C)

Two-Way Contingency Table (Observed)

Lithofacies Predict qXRD 064 & 077	L4	L3	L2a	L2	L2b	L1
L4	**21**	6	1	6	1	1
L3	0	**11**	1	1	1	0
L2a	0	0	**18**	9	6	0
L1	0	4	1	2	0	**11**
df = 15	Chisq = 149.40		p = < 0.0001			
	Chi-sq 0.01 = 30.58			C = 0.65		

D)

Two-Way Contingency Table (Observed)

Lithofacies predict qXRD & GS 064 and 074	L4	L3	L2a	L2	L2b	L1
L4	**18**	1	0	0	0	1
L3	3	**16**	0	2	1	0
L2a	0	3	**21**	0	0	3
L2	0	0	0	**15**	7	0
L2b						
L1	0	1	0	1	0	**8**
df = 20	Chi-sq 260.48		p = < 0.0001			
	Chi-sq: 0.01 = 37.57			C = 0.85		

Lajeunesse 2017), deposition on the slopes would have been dominated by erosion and transportation of sediments derived from the Baffin Island Archean and Paleoproterozoic outcrops (Jackson and Berman 2000; St-Onge et al. 2009).

We posit that the lithofacies sequence on the northern Baffin Island slope contains information on the retreat and deglaciation of the ice streams that flowed S and E into Baffin through Lancaster, Jones, and Smith sounds and Nares Strait (Figs. 1B, 7), but also includes sediments laterally sourced from Baffin Island (Jenner et al. 2018). We might expect that as the ice streams retreated, sites downstream from the ice fronts would record changes in the mineral composition and color of the bedrock (Fig. 1B). The precise timing of these events is rendered difficult because there is no consensus on an appropriate reservoir correction(s) (Coulthard et al. 2010; Jennings et al. 2011, 2019; Furze et al. 2018; Georgiadis et al. 2018). Ice retreat occurred from the ice fronts discharging through the CAC to the Arctic Ocean (Dyke et al. 2002; Jennings et al. 2011; Lakeman et al. 2018) and from an extensive margin in northern Baffin Bay (Li et al. 2011).

The most obvious evidence for the late Pleistocene deglaciation at sites 64 and 77 is the onset of the tan-carbonate deposition correlated to BBDC #1 #0, with the onset dated regionally in Baffin Bay at ca. 14.5 cal ka BP (Andrews et al. 1998; Simon et al. 2014; Jennings et al. 2017; Jenner et al. 2018). The separation of BBDC #1 and #0 is especially distinct in the 64 Ca/Ti XRF ratios (Jenner et al. 2018) but is also evident in the lithofacies and in the carbonate mineralogy. Tan carbonate muds are underlain by

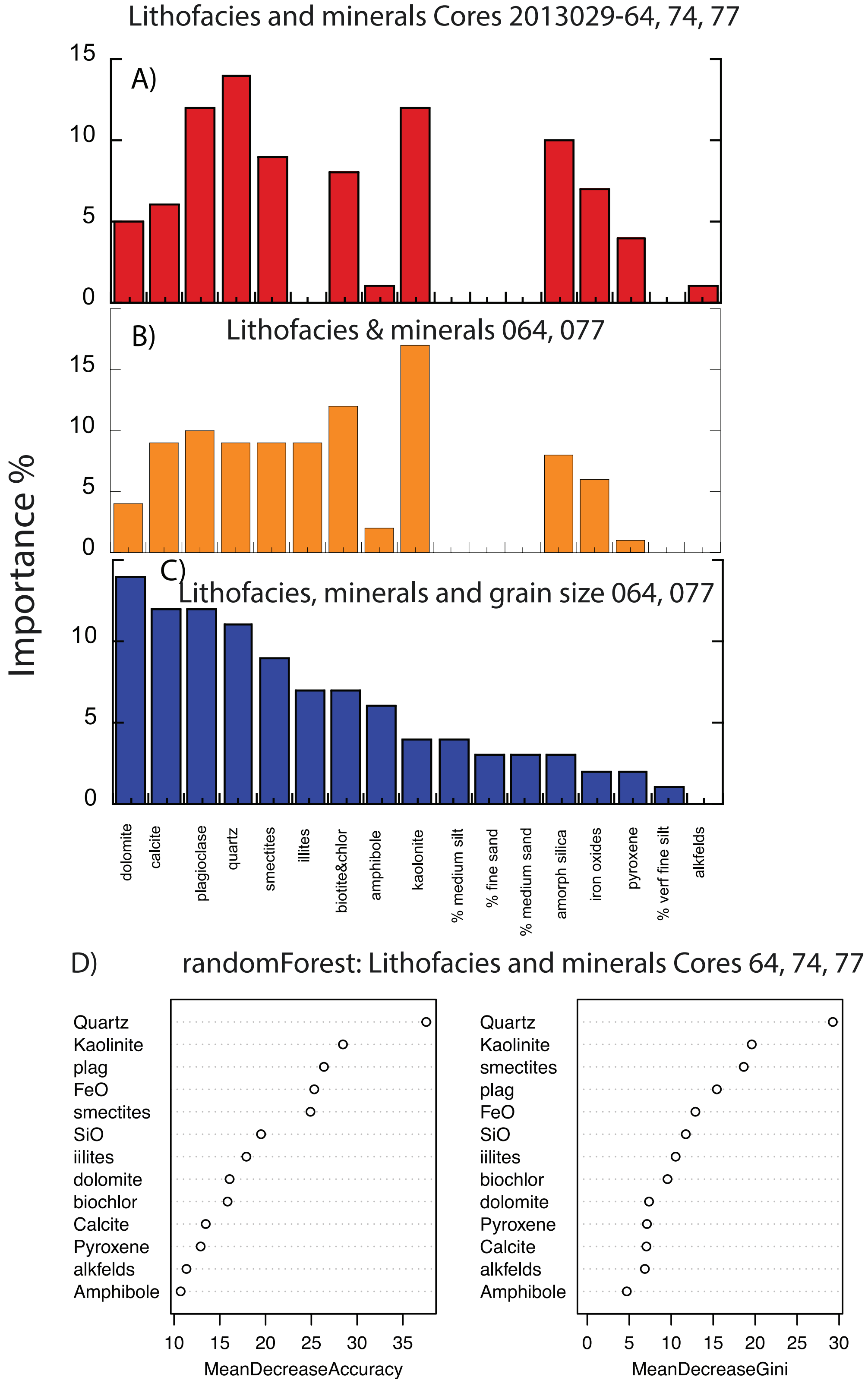

FIG. 5.—Measure of the importance of various minerals in the classification decision tree for: **A)** minerals in cores 64, 74, and 77, **B)** minerals for cores 64 and 77, **C)** minerals and grain size for cores 64 and 77, **D)** importance of the minerals in a "randomForest" analysis of the lithofacies and mineral data. The mean decrease in the Gini coefficient is a measure of "how each variable contributes to the homogeneity of the nodes and leaves." The analyses show slightly different results but emphasize the importance of quartz and kaolinite. Note that smectites and iron oxides increase in importance relative to the classification decision tree data (Fig. 5A, B).

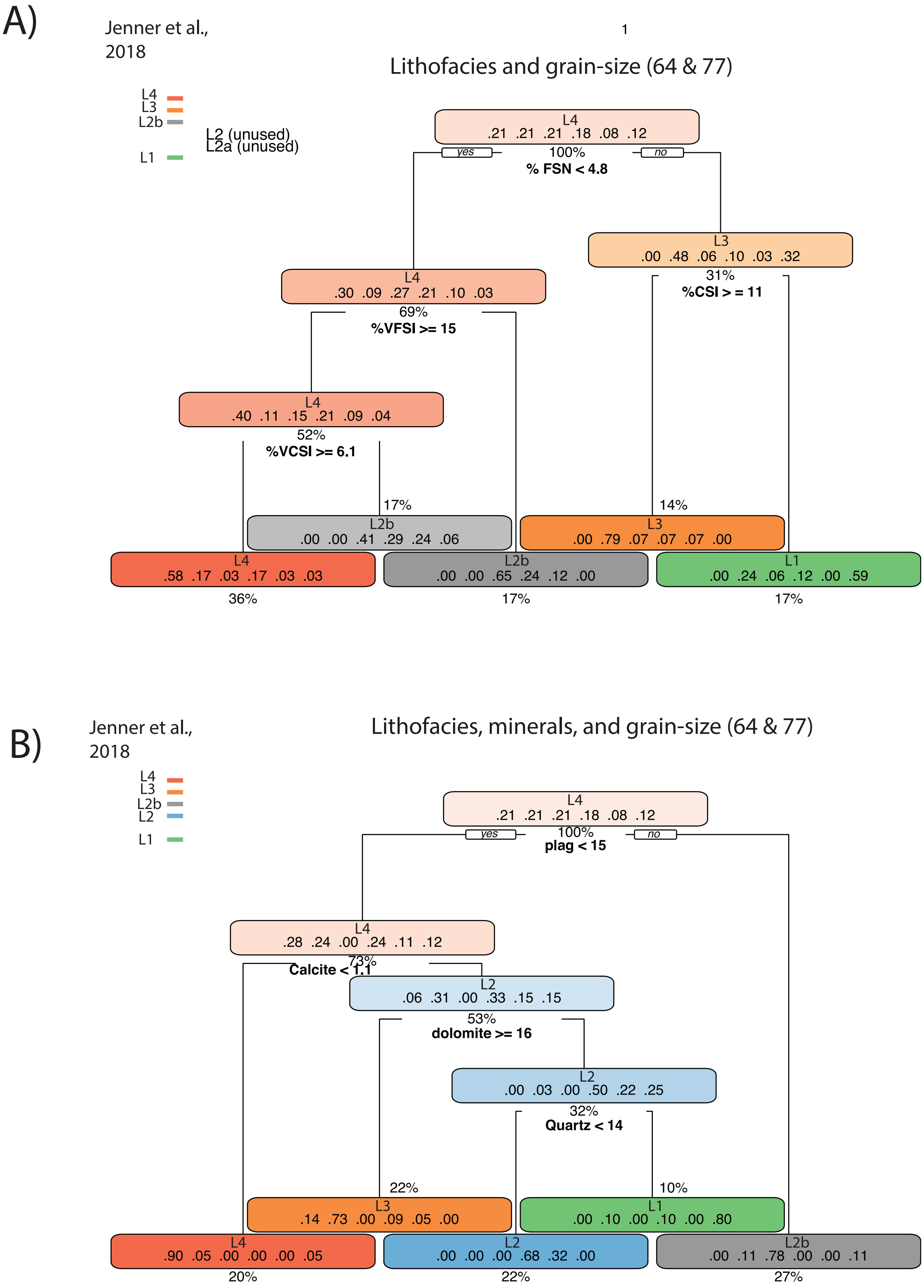

FIG. 6.—**A)** cp plot minerals and grain size. **B)** Classification decision tree for the association between lithology, minerals, and grain-size classes. **C)** Classification decision tree for the association between lithofacies and mineral and grain-size classes for cores 64 and 77.

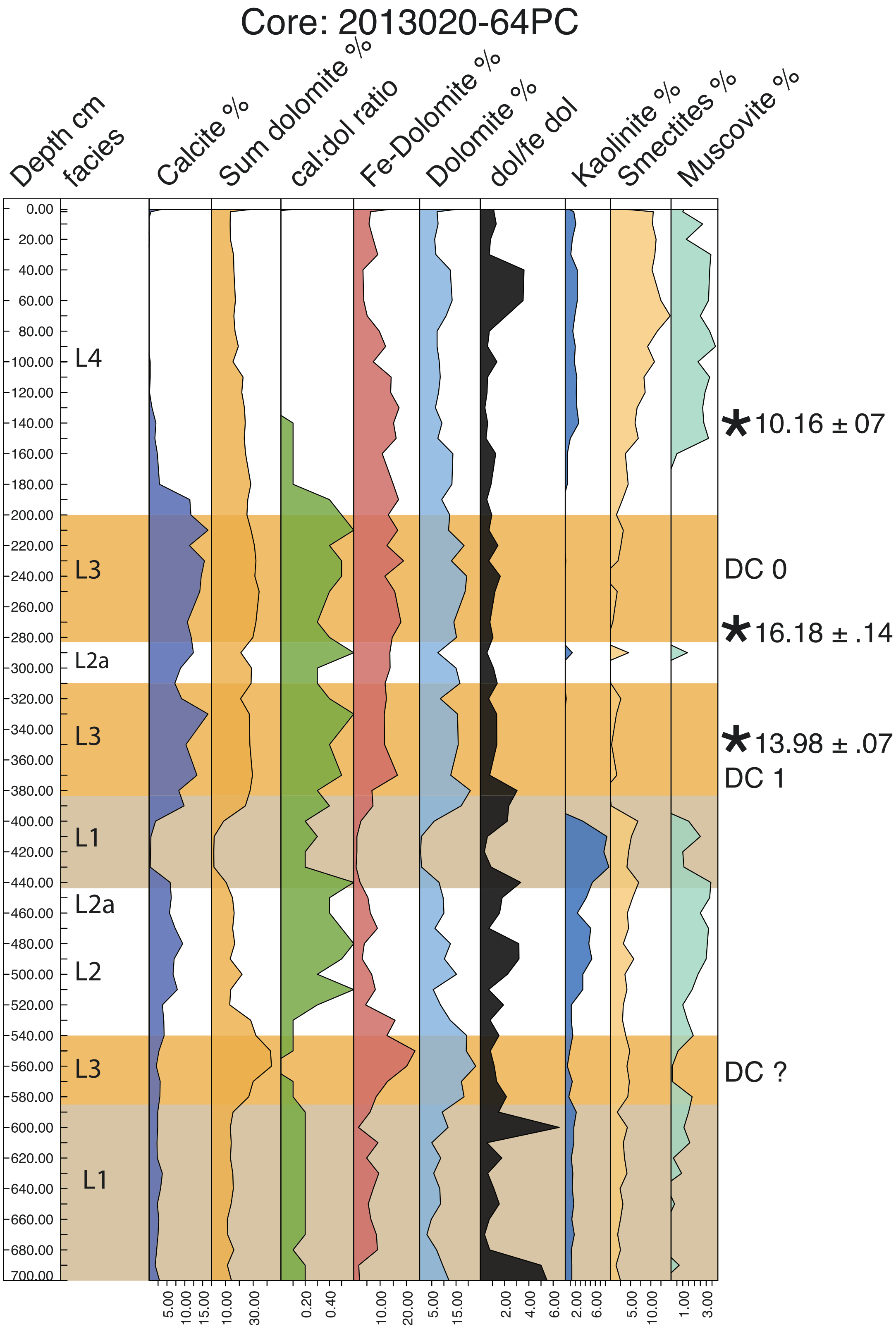

FIG. 7.—Downcore plot of the carbonate mineral wt% and ratios, weathering clays, and muscovite for core 20013029 64. The total dolomite wt% consist of dolomite ($CaMg(CO_3)_2$) and Fe-dolomite (ferroan dolomite ($Ca(Mg,Fe)(CO_3)_2$)).

TABLE 3.—Results of the *post hoc* Scheffe test on normalized (0 to 1) qXRD data showing the results of paired comparisons between the six lithofacies.

	Quartz		Kaolinite		Plagioclase		FeO		Smectite	
Lithofacies	p	Significant	p	Significant	p	Significant	p	Significant	p	Significant
Hm v Tan Cbtm	< 0.0001	Yes	< 0.0001	Yes	0.0899	No	< 0.0001	Yes	< 0.0001	Yes
Hm v Lt gm	0.0004	Yes	0.7601	No	< 0.0001	Yes	0.7601	No	< 0.0001	Yes
Hm v Rbm	0.0015	Yes	0.0003	Yes	0.999	No	0.0003	Yes	< 0.0001	Yes
HM v Gld BM	0.0322	Yes	0.003	Yes	0.6798	No	0.003	Yes	0.0006	Yes
Hm v Dmm	< 0.0001	Yes	0.8196	No	0.0003	Yes	0.8196	No	< 0.0001	Yes
Tan C btm v Lt gm	0.6402	No	< 0.0001	Yes	< 0.0001	Yes	< 0.0001	Yes	0.0001	Yes
Tan C btm v Rbm	0.3821	No	0.3056	No	0.2026	No	0.3056	No	0.0032	Yes
Tan C btm v Gld BM	0.2132	No	0.4839	No	0.725	No	0.4839	No	0.0026	Yes
Tan C btm v Dmm	< 0.0001	Yes	< 0.0001	Yes	0.0232	Yes	< 0.0001	Yes	0.2017	No
Lt gm v Rbm	0.8594	No	0.0029	Yes	< 0.0001	Yes	0.0029	Yes	0.2614	No
Lt gm v Gld BM	0.4933	No	0.0109	Yes	0.0002	Yes	0.0109	Yes	0.9694	No
Lt gm v Dmm	< 0.0001	Yes	0.9809	No	0.0006	Yes	0.9809	No	0.0011	Yes
Rbm v Gld BM	0.7313	No	0.9989	No	0.7529	No	0.9989	No	0.5153	No
Rbm v Dmm	< 0.0001	Yes	0.0009	Yes	0.003	Yes	0.0009	Yes	0.0289	Yes
Gld BM v Dmm	< 0.0001	Yes	0.0058	Yes	0.0468	Yes	0.0058	Yes	0.0148	Yes

	Lithofacies	# Difference
L4	Hm	21
L3	Tab Cbtm	16
L2b	Lt gm	15
L2	Rbm	13
L2a	Gld BM	11
L1	Dmm	21

laminated red-brown muds in cores 77 and 64. A thin diamicton separating red brown mud from tan carbonate mud in core 64 is interpreted as a possible, localized ice advance (Jenner et al. 2018). The subtle red tinge to L2 is likely associated with erosion of Baffin Island bedrock given the absence of a southward thinning of red-brown muds (which would be expected from a meltwater-derived northern source) and the relative thickening of red-brown muds seaward of Baffin Island troughs (Jenner et al. 2018). Jennings et al. (2019) recorded red laminated muds with IRD in core 2001LSSL-0014PC (Fig. 1) linked to erosion of sediments in the Thule Supergroup (Dawes 1997; Dawes et al. 2000) during ice-stream retreat into Smith Sound. The onset of these muds, however, is ~ 11 cal ka BP, younger than similar-looking red-brown muds from the western Baffin Bay margin which are dated between 41 and ~ 15 cal ka BP.

An additional tan carbonate DC event in core 64, between 540 and 580 cm, lies directly above the basal diamicton (L1) (Fig. 2, 8) (Jenner et al. 2018). In comparison with DC#0 and #1, this unit is characterized by a low calcite/dolomite ratio, which suggests either dissolution of fine-grained calcite or a carbonate bedrock source containing relatively little calcite. The three piston cores include the last DC event (DC-0), which ended before 9.6 cal ka BP (Jenner et al. 2018) and above the facies L4 (Fig. 2). These cores contains a regionally distinct, but not well dated, event (Knudsen et al. 2008; Andrews and Eberl 2011), which is the relatively abrupt cessation of detrital-calcite deposition (Fig. 7), caused by the onset of the introduction of Pacific-sourced surface water (Azetsu-Scott et al. 2010) and linked to the final opening of the CAC about 9 ± cal ka BP (Jennings et al. 2011, 2019). We have not investigated in detail changes in the mineral provenance in L4, although we expect that variations in mineral composition and grain size will be evident in response to the complex retreat of ice streams in the CAC (e.g., Belt et al. 2010; Furze et al. 2018; Georgiadis et al. 2018; Jennings et al. 2019; McCave and Andrews 2019b). However, there is no cessation in the occurrence of dolomite and ferrous dolomite in cores 64, 74, and 77, indicating continuous Holocene glacial erosion of Paleozoic outcrops in NW Greenland and elsewhere (Fig. 1B).

CONCLUSIONS

A series of distinct lithofacies, based on color and other visible attributes, have been described from three cores on the Baffin Island slope. We show that these lithofacies are well predicted by mineral compositions. The addition of grain-size data does not substantially increase the degree of predictability, but it substantially changed the percentage importance of the minerals in terms of the lithofacies classification. Our results demonstrate that lithofacies reflect change in both sediment provenance and transport processes and thus capture the changing environmental dynamics as the Greenland, Laurentide, and Innuitian ice sheets moved from full glacial to deglacial conditions at the end of the last major glacial cycle.

ACKNOWLEDGMENTS

JTA acknowledges the support of National Science Foundation grant #1804504, and Anna Klein and Wendy Roth for assistance in X-ray diffraction data and grain-size preparation. We acknowledge with thanks the various authors of the R-packages that were used as a critical part of this investigation (https://cran.r-project.org/web/packages/).

REFERENCES

AKSU, A.E., 1981, Late Quaternary stratigraphy, paleoenvironmentology, and sedimentation history of Baffin Bay and Davis Strait [PhD Dissertation]: Halifax, Dalhousie University, 771 p.

AKSU, A.E., 1985, Climatic and oceanographic changes over the past 400,000 years: evidence from deep-sea cores on Baffin Bay and Davis Strait, *in* Andrews, J.T., ed., Quaternary Environments: Eastern Canadian Arctic, Baffin Bay, and Western Greenland: Boston, Allen and Unwin, p. 181–209.

AKSU, A.E., AND HISCOTT, R.N., 1989, Slides and debris flows on the high-latitude continental slopes of Baffin Bay: Geology, v. 17, p. 885–888.

AKSU, A.E., AND MUDIE, P.J., 1984, Palaeoclimate of Baffin Bay from 300,000-year record of foraminifera, dinoflagellates, and pollen: Nature v. 312, p. 630–634.

AKSU, A.E., AND PIPER, D.J.W., 1987, Late Quaternary sedimentation in Baffin Bay: Canadian Journal of Earth Sciences, v. 24, p. 1833–1846.

ANDREWS, J.T., 2019, Baffin Bay–Nares Strait surface (seafloor) sediment mineralogy: further investigations and methods to elucidate spatial variations in provenance: Canadian Journal of Earth Sciences, v. 56, p. 814–828.

ANDREWS, J.T., AND EBERL, D.D., 2011, Surface (sea floor) and near-surface (box core) sediment mineralogy in Baffin Bay as a key to sediment provenance and ice sheet variations: Canadian Journal of Earth Sciences, v. 48, p. 1307–1328.

ANDREWS, J.T., AND ROTH, W.J., in prep, Sampling glacial marine sediment (core MD99-2317): questions and results of a within and between variable experiment.

ANDREWS, J.T., KIRBY, M.E., AKSU, A., BARBER, D.C., AND MEESE, D., 1998, Late Quaternary detrital carbonate (DC) events in Baffin Bay (67–74° N): Do they correlate with and contribute to Heinrich Events in the North Atlantic?: Quaternary Science Reviews, v. 17, p. 1125–1137.

ANDREWS, J.T., GIBB, O.T., JENNINGS, A.E., AND SIMON, Q., 2014, Variations in the provenance of sediment from ice sheets surrounding Baffin Bay during MIS 2 and 3 and export to the Labrador Shelf Sea: site HU2008029-0008 Davis Strait: Journal of Quaternary Science, v. 29, p. 3–13.

ANDREWS, J.T., BJORK, A.A., EBERL, D.D., JENNINGS, A.E., AND VERPLANCK, E.P., 2015, Significant differences in late Quaternary bedrock erosion and transportation: east versus west Greenland ~ 70°N and the evolution of glacial landscapes: Journal of Quaternary Science, v. 30, p. 452–463.

ANDREWS, J.T., KLEIN, A.J., JENNER, K., CAMPBELL, D.C., AND JENNINGS, A.E., 2018, The variability of Baffin Bay seafloor sediment mineralogy: the identification of discrete glacial sediment sources and application to late Quaternary downcore analysis: Canadian Journal of Earth Sciences, v. 55, p. 620–639.

Azetsu-Scott, K., Clarke, A., Falkner, K., Hamilton, J., Jones, E.P., Lee, C., Petrie, B., Prinsenberg, S., Starr, M., and Yeats, P., 2010, Calcium carbonate saturation states in the waters of the Canadian Arctic Archipelago and the Labrador Sea: Journal of Geophysical Research, Oceans, v. 115, C11021.

Belt, S.T., Vare, L.L., Masse, G., Manners, H.R., Price, J.C., MacLachlan, S.E., Andrews, J.T., and Schmidt, S., 2010, 2010, Striking similarities in temporal changes to spring sea ice occurrence across the central Canadian Arctic Archipelago over the last 7000 years: Quaternary Science Reviews, v. 29, p. 3489–3504.

Bennett, R., Campbell, D.C., Furze, M.F.A., and Haggart, J.W., 2014, The shallow stratigraphy and geohazards of the Northeast Baffin Shelf and Lancaster Sound: Bulletin of Canadian Petroleum Geology, v. 62, p. 217–231.

Blott, S.J., and Pye, K., 2001, GRADISTAT: a grain size distribution and statistics package for the analysis of unconsolidated sediments: Earth Surface Processes and Landforms, v. 26, p. 1237–1248.

Brouard, E., and Lajeunesse, P., 2017, Maximum extent and decay of the Laurentide Ice Sheet in Western Baffin Bay during the last glacial episode: Nature, Scientific Reports, v. 7, doi:10.1038/s41598-017-11010-9.

Coulthard, R.D., Furze, M.F.A., Pienkowski, A.J., Nixon, F.C., and England, J.H., 2010, New marine Delta R values for Arctic Canada: Quaternary Geochronology, v. 5, p. 419–434.

Dawes, P.R., 1997, The Proterozoic Thule Supergroup, Greenland and Canada: history, lithostratigraphy and development: Geology of Greenland Survey, Bulletin, v. 174, p. 1–24.

Dawes, P.R., Frisch, T., Garde, A.A., Ianelli, T.R., Ineson, J.R., Jensen, S.M., Pirajno, F., Stenmerik, L., Stouge, S., Thomasse, B., and van Gool, J., 2000, Kane Basin 1999: mapping, stratigraphic studies and econmoic assessment of Precambrian and Lower Paleozoic provinances in north-western Greenland: Geology of Greenland Survey Bulletin, v. 186, p. 11–28.

Dyke, A.S., Andrews, J.T., Clark, P.U., England, J.H., Miller, G.H., Shaw, J., and Veillette, J.J., 2002, The Laurentide and Innuitian ice sheets during the Last Glacial Maximum: Quaternary Science Reviews, v. 21, p. 9–31.

Eberl, D.D., 2003, User guide to RockJock: a program for determining quantitative mineralogy from X-ray diffraction data: U.S. Geological Survey, Open File Report 03-78, 40 p.

Furze, M.F.A., Pienkowski, A.J., McNeely, M.A., Bennett, R., and Cage, A.G., 2018, Deglaciation and ice shelf development at the northeast margin of the Laurentide Ice Sheet during the Younger Dryas chronozone: Boreas, v. 7, p. 271–296.

Georgiadis, E., Giraudeau, J., Martinez, P., Lajeunesse, P., St-Onge, G., Schmidt, S., and Masse, G., 2018, Deglacial to postglacial history of Nares Strait, Northwest Greenland: a marine perspective from Kane Basin: Climate of the Past, v. 14, p. 1991–2010.

Gorunescu, F., 2011, Classification and decision trees: Berlin, Springer, Data Mining, Intelligent Systems Reference Library, p. 159–183.

Hesse, R., 2016, Ice-proximal Labrador Sea Heinrich layers: a sedimentological approach: Canadian Journal of Earth Sciences, v. 53, p. 71–100.

Jackson, G.D., and Berman, R.G., 2000, Precambrian metamorphic and tectonic evolution of northern Baffin Island, Nunavut, Canada: The Canadian Mineralogist, v. 38, p. 399–421.

Jenner, K.A., Campbell, D.C., and Piper, D.J.W., 2018, Along-slope variations in sediment lithofacies and depositional processes since the Last Glacial Maximum on the northeast Baffin margin, Canada: Marine Geology, v. 405, p. 92–107.

Jennings, A.E., Sheldon, C., Cronin, T.M., Francus, P., Stoner, J., and Andrews, J., 2011, The holocene history of Nares Strait: transition from Glacial Bay to Arctic–Atlantic throughflow: Oceanography, v. 24, p. 26–41.

Jennings, A.E., Andrews, J.T., Cofaigh, Ó C., St-Onge, G., Sheldon, S., Belt, S.T., Cabedo-Sanz, P., and Hillaire-Marcel, C., 2017, Ocean forcing of ice sheet retreat in central west Greenland from LGM through eglaciation: Earth and Planetary Science Letters, v. 472, p. 1–13.

Jennings, A.E., Andrews, J.T., Ó Cofaigh, St-Onge, G., Belt, S., Cabedo-Sanz, P., Pearce, C., Hillaire-Marcel, C., and Campbell, C., 2018, Baffin Bay paleoenvironments in the LGM and HS1: resolving the ice-shelf question: Marine Geology, v. 402, p. 5–16.

Jennings, A.E., Andrews, J.T., Oliver, B., Walczak, M., and Mix, A.C., 2019, Retreat of the Smith Sound Ice Stream in the Early Holocene: Boreas, v. 48, p. 825–840.

Kabacoff, R.I., 2015, R in Action: data analysis and graphics with R, 2nd edition: Manning Publications, Shelter Island, New York, 579 p.

Knudsen, K.L., Stabell, B., Seidenkrantz, M.S., Eiriksson, J., and Blake, W., 2008, Deglacial and Holocene conditions in northernmost Baffin Bay: sediments, foraminifera, diatoms and stable isotopes: Boreas, v. 37, p. 346–376.

Koseoglu, D., Belt, S.T., Husum, K., and Knies, J., 2018a, An assessment of biomarker-based multivariate classification methods versus the PIP25 index for paleo Arctic sea ice reconstruction: Organic Geochemistry, v. 125, p. 82–94.

Koseoglu, D., Belt, S.T., Smik, L., Yao, H.Y., Panieri, G., and Knies, J., 2018b, Complementary biomarker-based methods for characterising Arctic sea ice conditions: a case study comparison between multivariate analysis and the PIP25 index: Geochimica Et Cosmochimica Acta, v. 222, p. 406–420.

Lakeman, T.R., Pienkowski, A.J., Nixon, F.C., Furze, M.F.A., Blasco, S., Andrews, J.T., and King, E.L., 2018, Collapse of a marine-based ice stream during the early Younger Dryas chronozone, western Canadian Arctic: Geology, v. 46, p. 211–214.

Li, G., Piper, D.J.W., and Campbell, D.C., 2011, The Quaternary Lancaster Sound trough-mouth fan, NW Baffin Bay: Journal of Quaternary Science, v. 26, p. 511–522.

MacLean, B., Blasco, S., Bennett, R., England, J., Rainey, W., Hughes-Clarke, J., and Beaudoin, J., 2010, Ice keel seabed features in marine channels of the central Canadian Arctic Archipelago: evidence for former ice streams and iceberg scouring: Quaternary Science Reviews, v. 29, p. 2280–2301.

MacLean, B., Williams, G., and Zang, S., 2011, Cretaceous strata on the Baffin Island Shelf: Halifax, American Association of Petroleum Geologists, 3P Arctic–Polar Petroleum Potential Conference and Exhibition.

MacLean, B., Williams, G., and Zhang, S., 2014, New insights into the stratigraphy and petroleum potential of the Baffin shelf's Cretaceous rocks: Bulletin of Canadian Petroleum Geology, v. 62, p. 289–310.

Margold, M., Stokes, C.R., Clark, C.D., and Kleman, J., 2014, Ice streams in the Laurentide Ice Sheet: a new mapping inventory: Journal of Maps, v. 11, p. 380–385.

Margold, M., Stokes, C.R., and Clark, C.D., 2015a, Ice streams in the Laurentide Ice Sheet: identification, characteristics and comparison to modern ice sheets: Earth Science Reviews, v. 143, p. 117–146.

Margold, M., Stokes, C.R., Clark, C.D., and Kleman, J., 2015b, Ice streams in the Laurentide Ice Sheet: a new mapping inventory: Journal of Maps, v. 11, p. 380–395.

Marshall, S.J., and Clarke, G.K.C., 1996, Geologic and topographic controls on fast flow in the Laurentide and Cordilleran Ice Sheets: Journal of Geophysical Research, v. 101, p. 17,827–17,839.

McCave, I.N., and Andrews, J.T., 2019a, Distinguishing current effects in sediments delivered to the ocean by ice. I. Principles, methods and examples: Quaternary Science Reviews, v. 212, p. 92–107.

McCave, I.N., and Andrews, J.T., 2019b, Distinguishing current effects in sediments delivered to the ocean by ice. II. Glacial to Holocene changes in North Atlantic high latitude upper ocean flows: Quaternary Science Reviews, v. 223, 21p.

McCave, I.N., Thornalley, D.J.R., and Hall, I.R., 2017, Relation of sortable silt grain size to deep-sea current speeds: calibration of the "Mud Current Meter:" Deep-Sea Research Part I, Oceanographic Research Papers, v. 127, p. 1–12.

Miesch, A.T., 1976, Q-Mode factor analysis of compositional data: Computers & Geosciences, v. 1, p. 147–159.

Parnell, J., Bowden, S., Taylor, C., and Andrews, J.T., 2007, Biomarker determination as a provenance tool for detrital carbonate events (Heinrich events?): fingerprinting Quaternary glacial sources in Baffin Bay: Earth and Planetary Science Letters, v. 257, p. 71–82.

Piper, D.J.W., 1973, A Late Quaternary stratigraphic marker in the central basin of Baffin Bay: Maritime Sediments, v. 9, p. 62–63.

Prins, M.A., Bouwer, L.M., Beets, C.J., Troelstra, S.R., Weltje, G.J., Kruk, R.W., Kruijpers, A., and Vroon, P.Z., 2002, Ocean circulation and iceberg discharge in the glacial North Atlantic: inferences from unmixing of sediment sizes: Geology, v. 30, p. 555–558.

Raven, M.D., and Self, P.G., 2017, Outcomes of 12 years of the Reynolds Cup quantitative mineral analysis round robin: Clays and Clay Minerals, v. 65, p. 122–134.

Rebesco, M., Hernandez-Molina, F.J., Van Rooij, D., and Wahlin, A., 2014, Contourites and associated sediments controlled by deep-water circulation processes: state-of-the-art and future considerations: Marine Geology, v. 352, p. 111–154.

Siegel, S., 1956, Nonparamteric statistics: New York, McGraw-Hill, 312 p.

Simon, Q., Hillaire-Marcel, C., St-Onge, G., and Andrews, J.T., 2014, North-eastern Laurentide, western Greenland, and southern Innuitian ice stream dynamics during the last glacial cycle: Journal of Quaternary Science, v. 29, p. 14–26.

St-Onge, M.R., van Gool, J.A.M., Garde, A.A., and Scott, D.J., 2009, Correlation of Archaean and Palaeoproterozoic units between northeastern Canada and western Greenland: constraining the pre-collisional upper plate accretionary history of the Trans-Hudson orogen: Earth Accretionary Systems in Space and Time, v. 318, p. 193–235, doi:10.1144/SP318.7.

Vermeesch, P., 2006, Tectonic discrimination of basalts with classification trees: Geochimica et Cosmochimica Acta, v. 70, p. 1839–1848.

Zumel, N., and Mount, J., 2014, Practical Data Science with R: Manning Publications, Shelter Island, New York, 568 p.

Received 24 October 2019; accepted 13 April 2020.

Queries for sedp-90-07-04

This article has been typeset from the submitted materials. Check proofs carefully for conversion or other inadvertent errors. Please follow the Allen Press Guide to PDF Annotation when marking revisions. Do not edit the PDF directly.

If present, queries will be listed below with corresponding numbers in the margins or may appear as PDF comments addressed to the author or editor. If a correction is desired in response to a query, mark the necessary changes directly in the proof using the appropriate annotation tool. If no change is desired, no action is necessary in response.